




Self-Supervised Learning for Image Super-Resolution and Deblurring

Jérémy Scanvic^{1,2} , Mike Davies¹ , Patrice Abry² , and Julián Tachella² 

¹ School of Engineering, University of Edinburgh
Edinburgh, EH9 3FB, UK

² Laboratoire de Physique, CNRS, ENSL
Lyon, F-69364, France

Abstract. Self-supervised methods have recently proved to be nearly as effective as supervised methods in various imaging inverse problems, paving the way for learning-based methods in scientific and medical imaging applications where ground truth data is hard or expensive to obtain. This is the case in magnetic resonance imaging and computed tomography. These methods critically rely on invariance to translations and/or rotations of the image distribution to learn from incomplete measurement data alone. However, existing approaches fail to obtain competitive performances in the problems of image super-resolution and deblurring, which play a key role in most imaging systems. In this work, we show that invariance to translations and rotations is insufficient to learn from measurements that only contain low-frequency information. Instead, we propose a new self-supervised approach that leverages the fact that many image distributions are approximately scale-invariant, and that enables recovering high-frequency information lost in the measurement process. We demonstrate throughout a series of experiments on real datasets that the proposed method outperforms other self-supervised approaches, and obtains performances on par with fully supervised learning ³.

Keywords: Image Deblurring · Image Super-Resolution · Self-Supervised Learning

1 Introduction

Inverse problems are ubiquitous in scientific imaging and medical imaging. Linear inverse problems are generally modeled by the forward process

$$y = Ax + \varepsilon, \tag{1}$$

where $y \in \mathbb{R}^m$ represents the observed measurements, $x \in \mathcal{X} \subset \mathbb{R}^n$ represents the signal, $A \in \mathbb{R}^{m \times n}$ is the forward operator, and $\varepsilon \in \mathbb{R}^m$ depicts the noise

³ The code is available at <https://github.com/jscanvic/Scale-Equivariant-Imaging>

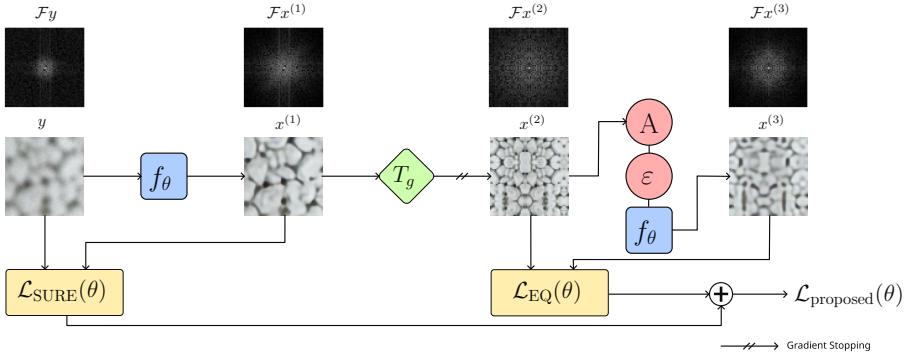


Fig. 1: Solving image super-resolution and deblurring without ground truth images. Our method consists in training a deep neural network f_θ to learn the reconstruction function $f : y \mapsto x$ using noisy measurements $y = Ax + \epsilon$ only, by minimizing a new self-supervised loss $\mathcal{L}_{\text{proposed}}(\theta)$ which leverages the scale-invariance property of common signal distributions. The loss is the sum of the SURE loss $\mathcal{L}_{\text{SURE}}(\theta)$ which penalizes reconstruction error in the measurement domain, and of the equivariant loss $\mathcal{L}_{\text{EQ}}(\theta)$ by viewing $x^{(1)} = f_\theta(y)$ as a ground truth which might lack high-frequency content, and the downsampled image $x^{(2)} = T_g x^{(1)}$ as another one which has high-frequency content, and finally by penalizing the mean squared error of the reconstruction $x^{(3)}$ obtained from a noisy measurement of $x^{(2)}$. The difference in high-frequency content is shown by $\mathcal{F}x^{(1)}$ and $\mathcal{F}x^{(2)}$, where \mathcal{F} is the discrete Fourier transform. One of our key contributions is stopping the gradient of $x^{(2)}$ during the stochastic gradient descent (see Section 4 for details).

corrupting the measurements. In this paper, we focus on additive white Gaussian noise but our results can easily be generalized for other noise distributions, e.g. Poisson, or mixed Gaussian-Poisson. Recovering x from the noisy measurements is generally ill-posed. In many cases, the forward operator is rank-deficient, e.g. when the number of measurements is less than the number of image pixels, that is $m < n$. Moreover, even when the forward operator is not rank-deficient, it might still be ill-conditioned, and reconstructions might be very sensible to noise (e.g., in image deblurring problems).

There is a wide range of approaches for solving the inverse problem, i.e., recovering x from y . Classical methods rely on hand-crafted priors, e.g. a total variation, together with optimization algorithms to obtain a reconstruction that agrees with the observed measurements and the chosen prior [7, 11]. These model-based approaches often obtain suboptimal results due to a mismatch between the true image distribution and the hand-crafted priors. An alternative approach leverages a dataset of reference images and associated measurements in order to train a reconstruction model. While this approach generally obtains state-of-the-art performance, it is often hard to apply it in problems where ground truth images are expensive or even impossible to obtain.

In recent years, self-supervised methods have highlighted the possibility of learning from measurement data alone, thus bypassing the need for ground truth references. These methods focus either on taking care of noisy data or a rank-deficient operator. Noise can be handled through the use of Stein’s unbiased risk estimator if the noise distribution is known [27], or via Noise2x techniques [3, 22, 23] which require milder assumptions on the noise distribution such as independence across pixels [3]. Rank-deficient operators can be handled using measurement data associated with multiple measurement operators A_1, \dots, A_G (each with a different nullspace) [6, 37], or by assuming that the image distribution is invariant to certain groups of transformations such as translations or rotations [8, 9].

Self-supervised image deblurring methods have been proposed for deblurring with multiple (known) blur kernels [29], however this assumption is not verified in many applications. Moreover, self-supervised methods that rely on a single operator (e.g., a single blur kernel) [8, 9], have not been applied to inverse problems with a single forward operator that removes high-frequency information such as image super-resolution and image deblurring, except for methods exploiting internal/external patch recurrence [34] which assume noiseless measurements, thus not being easily generalizable to other inverse problems.

Image deblurring and super-resolution are two inverse problems particularly difficult to solve using self-supervised methods. The former is severely ill-conditioned, and the latter is rank-deficient. This makes methods that minimize the measurement consistency error inapplicable as they cannot retrieve any information that lies within the nullspace [8] or where the forward operator is ill-conditioned, whenever there is even the slightest amount of noise present.

In this work, we propose a new self-supervised loss for training reconstruction networks for super-resolution and image deblurring problems which relies on the assumption that the underlying image distribution is scale-invariant, and can be easily applied to any linear inverse problem, as long as the forward process is known. Figure 1 shows an overview of that loss. The main contributions are the following:

1. We propose a new self-supervised loss based on scale-invariance for training reconstruction networks, which can be applied to any linear inverse problem where high-frequency information is lost by the forward operator.
2. Throughout a series of experiments, we show that the proposed method outperforms other self-supervised learning methods, and obtains a performance on par with fully supervised learning.

2 Related work

Supervised image reconstruction Most state-of-the-art super-resolution and image deblurring methods rely on a dataset containing ground truth references [13, 24, 33, 41]. However, in many scientific imaging problems such as fluorescence microscopy and astronomical imaging, having access to high-resolution images can be difficult, or even impossible [4].

Prior-based approaches A family of super-resolution and image deblurring methods rely on plug-and-play priors [20] and optimization methods. Other approaches rely on the inductive bias of certain convolutional architectures, i.e., the deep image prior [32, 39]. There are other methods that combine both techniques [26]. However, these approaches can provide sub-optimal results if the prior is insufficiently adapted to the problem.

SURE Stein’s unbiased risk estimator is a popular strategy for learning from noisy measurement data alone, which requires knowledge of the noise distribution [14, 27, 35]. However, for image super-resolution and image deblurring, the forward operator is typically either rank-deficient or at least severely ill-conditioned, and the SURE estimates can only capture discrepancies in the range of the forward operator.

Noise2x methods The Noise2Noise method [23] shows that it is possible to learn a denoiser in a self-supervised fashion if two independent noisy realizations of the same image are available for training, without explicit knowledge of the noise distribution. Related methods extend this idea to denoising problems where a single noise realization is available, e.g. Noise2Void [22] and Noise2Self [3], and to general linear inverse problems, e.g., Noise2Inverse [18]. However, all of these methods crucially require that the forward operator is invertible and well-conditioned, which is not the case for super-resolution and most deblurring problems.

Equivariant imaging The equivariant imaging (EI) method leverages the invariance of typical signal distributions to rotations and/or translations to learn from measurement data alone, in problems where the forward operator is incomplete such as sparse-angle tomography, image inpainting and magnetic resonance imaging [8, 9, 15]. However, this approach requires the forward operator to not be equivariant to the rotations or translations. The super-resolution problems and image deblurring problems with an isotropic blur kernel do not verify this condition, and EI methods cannot be used.

Patch recurrence methods Internal patch recurrence of natural images can be exploited to learn to super-resolve images without high-resolution references [34]. However, while this self-supervised learning method can be extended to collections of low-resolution images via external patch recurrence, it cannot be easily generalized to more general inverse problems (e.g., image deblurring) and noisy measurement data. The method proposed in this work generalizes the idea of patch recurrence to scale-invariance and can be applied to any imaging inverse problem where high-frequency information is missing.

3 Background

In this section, we review existing supervised and self-supervised learning approaches for the problems of image super-resolution and image deblurring. We

focus on reconstruction methods that train a reconstruction network $f_\theta : y \mapsto x$ which maps a low-resolution or blurry measurement y to a high-resolution image x .

Super-resolution and image deblurring The problem of image super-resolution consists in restoring a high-resolution image from a low-resolution one. It can be viewed as a linear inverse problem whose forward operator is defined by $Ax = (k * x) \downarrow_j$; where $*$ is the convolution operator⁴, $k \in \mathbb{R}^n$ is an antialiasing kernel, and \downarrow_j is the downsampling operator which keeps 1 every j pixels in the vertical and horizontal directions. The problem of image deblurring consists in restoring a sharp image from a blurry one defined by $Ax = k * x$, where $k \in \mathbb{R}^n$ is a blur kernel. In both problems, we assume that the measurements are corrupted by i.i.d. Gaussian noise of standard deviation σ .

Supervised loss Supervised methods typically consist in minimizing a loss which is meant to enforce $f_\theta(y) = x$ for all $x \in \mathcal{X} \subset \mathbb{R}^n$, i.e.

$$\mathcal{L}_{\text{SUP}}(\theta) = \sum_{i=1}^N \|f_\theta(y_i) - x_i\|_2^2. \quad (2)$$

Although the supervised loss is expressed here in terms of the ℓ^2 -norm, other losses such as the ℓ^1 -norm are sometimes preferred [24]. While most methods adopt this approach (often including other perceptual losses [5]), they cannot be applied to the setting where high-resolution targets x_i are not available.

Self-supervision via patch recurrence Inspired by the zero-shot super-resolution [34] and Noisier2Noise [28] methods, it is possible to use the measurements y_i as ground truth targets, and compute corresponding corrupted inputs applying the forward operator to y , i.e.,

$$z = Ay + \tilde{\varepsilon} \quad (3)$$

where $\tilde{\varepsilon}$ is sampled from a zero-mean Gaussian distribution with the same standard deviation. Then, a self-supervised loss is constructed as

$$\mathcal{L}_{\text{CSS}}(\theta) = \sum_{i=1}^N \|y_i - f_\theta(z_i)\|_2^2 \quad (4)$$

which we name Classic Self-Supervised (CSS) loss. This approach is only valid when measurements y can be interpreted as images, such as in a super-resolution problem [34], however, it is unclear whether it is effective for solving general problems, e.g. compressed sensing.

This method has been shown to be very effective in super-resolution problems [34] where the signal distribution is scale-invariant. However, this approach is not well-adapted to problems with arbitrary blurring kernels, where the measurements are far from ground truth images, even if the signal distribution is approximately scale-invariant.

⁴ We consider circular convolution for simplicity's sake.

Stein’s unbiased risk estimator The SURE loss [9, 27] is a self-supervised loss that serves as an unbiased estimator of the mean squared error (MSE) in measurement space

$$\mathbb{E}_{x,y} \left[\|Af_\theta(y) - Ax\|_2^2 \right], \quad (5)$$

which does not require access to ground truth signals x . The SURE loss for measurements corrupted by Gaussian noise of standard deviation σ [9] is given by:

$$\mathcal{L}_{\text{SURE}}(\theta) = \sum_{i=1}^N \frac{1}{m} \|Af_\theta(y_i) - y_i\|_2^2 + \sigma^2 - \frac{\sigma^2}{m} \sum_{i=1}^m \frac{\delta f_i}{\delta y_i}(y). \quad (6)$$

In practice, we approximate the divergence term using a Monte-Carlo estimate [31].

It is worth noting that, in the noiseless setting, i.e. $\sigma = 0$, the SURE loss is equal to a measurement consistency constraint, $Af_\theta(y) = y$

$$\mathcal{L}_{\text{MC}}(\theta) = \sum_{i=1}^N \frac{1}{m} \|Af_\theta(y_i) - y_i\|_2^2. \quad (7)$$

This loss does not penalize the reconstructions in the nullspace of A . In the setting of super-resolution and image deblurring, the nullspace of the operator is associated with the high-frequencies of the image x , and thus training against the SURE loss alone fails to reconstruct the high-frequency content.

Equivariant imaging The equivariant imaging approach [8], offers a way to learn in the nullspace of the operator A , by leveraging some prior knowledge about the invariances of the signal distribution. If the support of the signal distribution, i.e. the signal set \mathcal{X} , is invariant to a group of transformations $\{T_g\}_{g=1}^G$, then we have that for any signal x , $x' = T_g x$ also is a valid signal, and thus a measurement $y = Ax$ can also be interpreted as $y = A_g x'$ where $A_g = AT_g$ is a forward operator that might differ from A . This simple observation provides *implicit* access to a family of operators $\{AT_g\}_{g=1}^G$, which might have different nullspaces.

A necessary condition for learning is that A is not equivariant to the transformations [37]. Unfortunately, for imaging problems such as super-resolution and image deblurring, the forward operator A is equivariant to a group of rotations and/or translations T_g , which means there is not enough information for learning in the nullspace of A . We formalize this observation with the following propositions:

Proposition 1. *A blur operator with an isotropic kernel k is equivariant to translations and rotations.*

Proposition 2. *A downsampling operator with an ideal anti-aliasing filter k is equivariant to translations and rotations.*

We provide the proofs for both propositions in the appendix. This result leads us to choose downscaling transformations, for which both forward operators are not equivariant. Downscale transformations constitute a semigroup (there are no inverse operations) acting on idealized bandlimited (digital) images [16, 40]. In particular, for such digital images, the associated upscaling transformations do not provide proper inverses. Fortunately, although the blur and downsampling operators are equivariant to shifts and rotations, both are not equivariant to downscalings:

Theorem 1. *Consider the action by a semigroup of downscaling transformations with circular padding $\{T_g\}$ with scales $g \in \{1/2, 1/3, \dots\}$. If the forward operator A is a blur operator with an isotropic kernel or a downsampling operator with an ideal anti-aliasing filter, then it is not equivariant to downscalings.*

The proof is included in the appendix.

4 Proposed method

In order to solve the problems of image super-resolution and image deblurring, we train a deep neural network as the reconstruction function $f_\theta : y \mapsto x$, with learnable weights $\theta \in \mathbb{R}^p$. We propose to minimize the training loss

$$\mathcal{L}_{\text{proposed}}(\theta) = \mathcal{L}_{\text{SURE}}(\theta) + \alpha \mathcal{L}_{\text{EQ}}(\theta), \quad (8)$$

where $\alpha > 0$ is a trade-off parameter, $\mathcal{L}_{\text{SURE}}(\theta)$ is given in Equation (6), and $\mathcal{L}_{\text{EQ}}(\theta)$ is the equivariant loss introduced below, which is similar to the robust equivariant imaging loss [9]. In all experiments, we set $\alpha = 1$. The two contributions of our method are the use of the action by downscaling transforms instead of the action by shifts or by rotations, and stopping the gradient during the forward pass (details are explained below).

In the forward pass, we first compute $x_{i,\theta}^{(1)} = f_\theta(y_i)$, which we view as an estimation of the ground truth signal x . Next, we compute $x_i^{(2)} = T_g x_{i,\theta}^{(1)}$, where T_g is a downscale transformation of scale g , without propagating the gradient, which effectively leaves $\nabla_\theta x_i^{(2)} = 0$. Finally, we compute $x_{i,\theta}^{(3)} = f_\theta(Ax_i^{(2)} + \tilde{\varepsilon})$ where $\tilde{\varepsilon}$ is sampled from $\mathcal{N}(0, \sigma^2 I)$. The three terms are used to compute $\mathcal{L}_{\text{SURE}}$ and \mathcal{L}_{EQ} (see Figure 1), where \mathcal{L}_{EQ} is defined as

$$\mathcal{L}_{\text{EQ}}(\theta) = \sum_{i=1}^N \frac{1}{n} \|x_{i,\theta}^{(3)} - x_i^{(2)}\|_2^2. \quad (9)$$

Downscale transformations In all experiments, T_g consists in resampling the input image viewed as periodic on a (coarse) grid with a spacing of $1/g$ pixels, using bicubic interpolation. The grid center is chosen randomly at each call and the scale factor is chosen uniformly from $\{.5, .75\}$. Figure 2 shows two possible downscalings of an image patch.

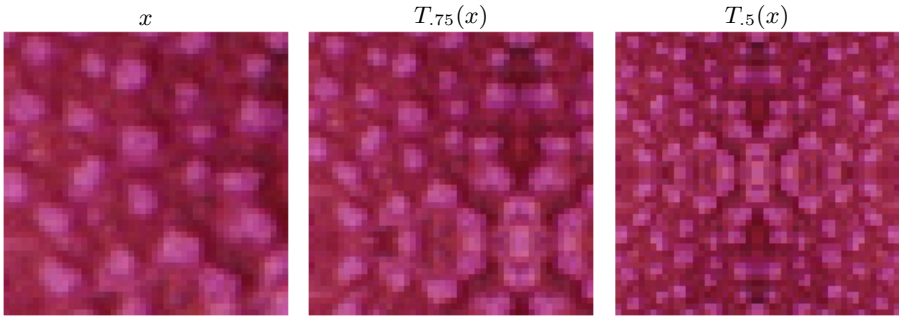


Fig. 2: Scale transform. An image x and downsampled images $T_{.75}(x)$ and $T_{.5}(x)$.

Gradient stopping The gradient-stopping step, which removes the dependence of $x_i^{(2)}$ on the network weights θ plays an important role in the self-supervised loss. Table 4 shows that gradient stopping significantly improves the performance of the self-supervised network for both image deblurring and image super-resolution, i.e. by about 1dB. Such gradient-stopping steps have proved crucial in various self-supervised representation learning methods and lead to significant performance increase [10, 17].

Comparison to self-supervision via patch recurrence Both the proposed loss and the CSS loss in (4) leverage scale-invariance to form a self-supervised loss. The CSS method requires that A is a downsampling transformation and that the noise ε is sufficiently small, such that $Ay \approx x'$ for some x' which also belongs to the dataset. The proposed method exploits scale-invariance on the reconstructed images, thus being applicable to any operator A . Thus, for the super-resolution problems with a small amount of noise, we expect to obtain a similar performance with both methods, whereas in the more challenging image deblurring problem we expect to observe a different performance across methods.

5 Experiments

Div2K Dataset Throughout the experiments, we use a synthetic dataset containing pairs of ground truth images and noisy measurements. Ground truth images are obtained from Div2K [1], a dataset containing high-resolution images (around 1500×1500 pixels) depicting natural scenes (e.g. buildings, landscapes, animals), which we resize to a resolution of around 300×300 pixels in image deblurring experiments, in order to get significant degradation with reasonably small kernels. For image super-resolution, we use MATLAB’s `imresize` function, a downsampling function with a bicubic anti-aliasing filter; and for image deblurring they are obtained using circular convolution with a certain kernel, e.g. a Gaussian kernel or a box kernel. We denote the blur level by R_{blur} , corresponding to the standard deviation for Gaussian kernels and to the radius for

box kernels. The noisy measurements are then obtained from the clean ones by applying additive white Gaussian noise with standard deviation σ . The resulting dataset contains 900 pairs, 100 of which are put aside in a test split and are crucially not used for training, while the other 800 are. During training, we use pairs of random crops instead of full images (48×48 pixels each).

Network architecture To ensure a fair comparison, every model is built upon the same state-of-the-art image-reconstruction architecture, namely SwinIR [24]. Noisy measurements are processed by a series of convolutional, multi-head self-attention and multi-layered perceptron (MLP) layers, resulting in an estimate of the ground truth image. In image super-resolution experiments, an optional upsampling module is present. In total, it has around 11 million parameters.

Performance metrics We measure the performance of each method by computing both the average PSNR and SSIM between test images and estimates obtained from the noisy measurements. We compute the metrics on the luminance channel (Y) in the YCbCr color representation, as is often done when dealing with images having multiple channels [24].

Method	$R_{\text{blur}} = 2$		$R_{\text{blur}} = 3$		$R_{\text{blur}} = 4$	
	PSNR	SSIM	PSNR	SSIM	PSNR	SSIM
Supervised	29.0 ± 2.9	0.879 ± 0.052	27.2 ± 3.0	0.824 ± 0.073	25.4 ± 2.9	0.755 ± 0.089
Proposed	27.6 ± 2.6	0.847 ± 0.047	25.9 ± 2.8	0.776 ± 0.075	24.6 ± 2.7	0.713 ± 0.089
CSS	26.0 ± 2.8	0.804 ± 0.070	24.2 ± 2.8	0.712 ± 0.105	23.0 ± 2.7	0.638 ± 0.124
BM3D [11]	27.1 ± 2.7	0.809 ± 0.078	25.5 ± 2.8	0.743 ± 0.102	24.6 ± 2.8	0.700 ± 0.114
DIP [39]	24.0 ± 2.7	0.660 ± 0.091	22.9 ± 2.6	0.578 ± 0.104	22.1 ± 2.5	0.516 ± 0.102
y	23.3 ± 2.7	0.630 ± 0.101	21.9 ± 2.6	0.528 ± 0.129	21.0 ± 2.6	0.466 ± 0.140

Table 1: Reconstruction performance for box deblurring. Blurry images are denoted by $y = Ax + \epsilon$.

Training details We train models for 500 epochs against training losses \mathcal{L}_{SUP} , \mathcal{L}_{CSS} and $\mathcal{L}_{\text{proposed}}$. We use an initial learning rate of $2 \cdot 10^{-4}$ for super-resolution, and of $5 \cdot 10^{-4}$ for deblurring. We use a multi-step scheduler that divides the learning rate by a factor of 2 at epochs 250, 400, 450, and 475. We use a batch size of 16 for super-resolution, and of 8 for deblurring. We use the Adam optimizer [21] with $\beta = (.9, .99)$ and no weight decay. Models are trained on one GPU for about 20 hours for the proposed method, and about 10 hours for the supervised and CSS methods. The experiments are performed using a SIDUS solution [30].

Additional comparisons For both image deblurring and image super-resolution, we compare against Deep Image Prior (DIP) [39] which is used with shared



Fig. 3: Sample reconstructions for box deblurring. Blurry images are denoted by $y = Ax + \varepsilon$.

Method	$R_{\text{blur}} = 1$		$R_{\text{blur}} = 2$		$R_{\text{blur}} = 3$	
	PSNR	SSIM	PSNR	SSIM	PSNR	SSIM
Supervised	30.9 ± 2.8	0.929 ± 0.032	25.9 ± 2.8	0.803 ± 0.081	23.6 ± 2.8	0.694 ± 0.120
Proposed	30.3 ± 2.6	0.908 ± 0.031	25.8 ± 2.7	0.785 ± 0.081	23.5 ± 2.7	0.660 ± 0.122
CSS	29.1 ± 2.8	0.899 ± 0.040	24.2 ± 2.9	0.706 ± 0.110	22.8 ± 2.8	0.621 ± 0.137
BM3D [11]	29.5 ± 2.8	0.882 ± 0.052	25.4 ± 2.8	0.757 ± 0.094	23.5 ± 2.8	0.648 ± 0.131
DIP [39]	27.2 ± 2.8	0.818 ± 0.056	24.3 ± 2.8	0.678 ± 0.086	22.6 ± 2.7	0.561 ± 0.106
y	26.4 ± 2.6	0.795 ± 0.045	22.8 ± 2.6	0.598 ± 0.106	21.2 ± 2.5	0.494 ± 0.130

Table 2: Reconstruction performance for Gaussian deblurring. Blurry images are denoted by $y = Ax + \varepsilon$.

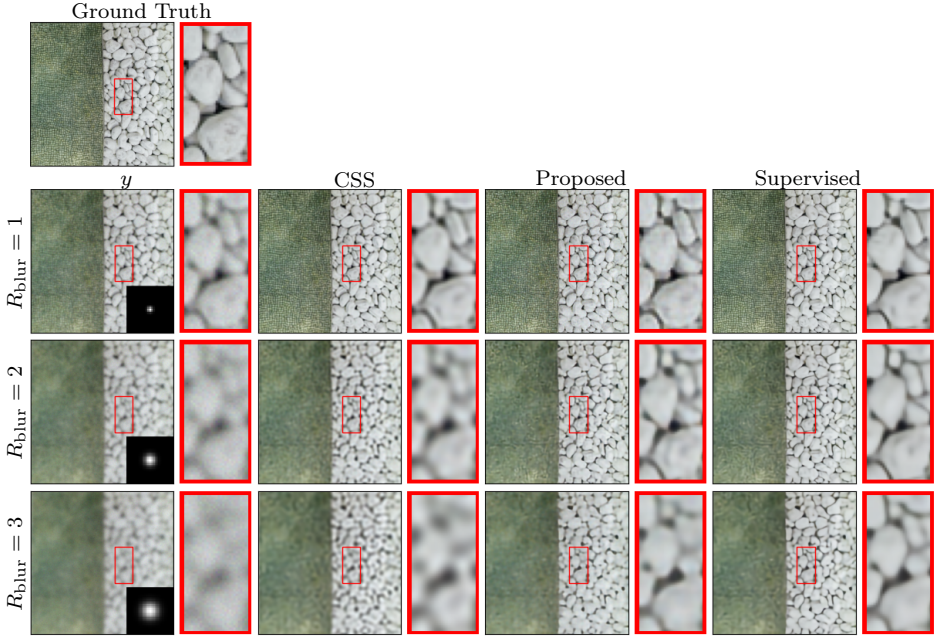


Fig. 4: Sample reconstructions for Gaussian deblurring. Blurry images are denoted by $y = Ax + \varepsilon$.

Method	Factor	σ	PSNR	SSIM	σ	PSNR	SSIM
Supervised	$\times 2$	0/255	34.7 ± 5.1	0.940 ± 0.045	25/255	29.3 ± 3.5	0.825 ± 0.078
Proposed			34.5 ± 5.0	0.939 ± 0.045		29.0 ± 3.4	0.813 ± 0.081
CSS			34.8 ± 5.0	0.940 ± 0.045		28.9 ± 3.1	0.786 ± 0.065
DIP [39]			23.1 ± 3.4	0.597 ± 0.152		23.0 ± 3.3	0.592 ± 0.152
$y \uparrow$			31.1 ± 4.7	0.896 ± 0.063		24.1 ± 1.2	0.472 ± 0.071
Supervised	$\times 4$	10/255	27.6 ± 4.1	0.769 ± 0.109	25/255	26.0 ± 3.6	0.716 ± 0.124
Proposed			27.1 ± 3.7	0.738 ± 0.100		25.7 ± 3.4	0.687 ± 0.122
CSS			27.4 ± 4.1	0.764 ± 0.109		25.9 ± 3.6	0.710 ± 0.122
DIP [39]			23.0 ± 3.3	0.588 ± 0.151		22.6 ± 3.1	0.572 ± 0.148
$y \uparrow$			25.6 ± 3.2	0.659 ± 0.095		22.6 ± 1.8	0.447 ± 0.059

Table 3: Reconstruction performance for image super-resolution. Low-resolution images $y = Ax + \varepsilon$ upscaled by bicubic interpolation are denoted by $y \uparrow$.

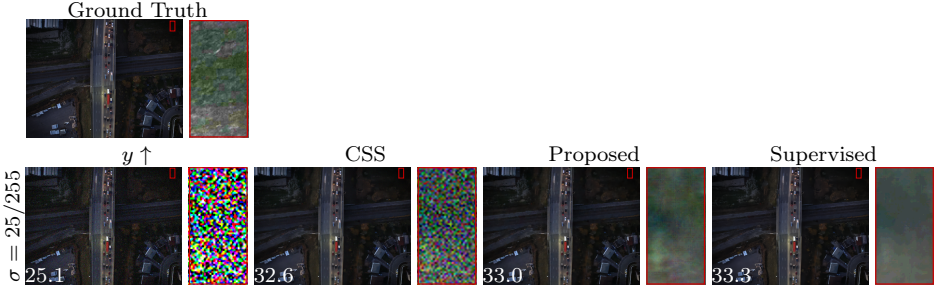


Fig. 5: Sample reconstructions for $\times 2$ image super-resolution. Low-resolution images $y = Ax + \varepsilon$ upscaled by bicubic interpolation are denoted by $y \uparrow$. PSNR is displayed in the bottom left corner of every high-resolution estimate.

Transform	Stop	Deblurring		Super-Resolution	
		PSNR	SSIM	PSNR	SSIM
Scale	✓	25.8 ± 2.7	0.785 ± 0.081	29.0 ± 3.4	0.813 ± 0.081
	×	24.0 ± 2.9	0.694 ± 0.114	28.0 ± 3.7	0.780 ± 0.098
Shift	✓	24.5 ± 2.6	0.728 ± 0.074	28.4 ± 3.2	0.773 ± 0.076
	×	23.0 ± 2.4	0.686 ± 0.119	28.5 ± 3.6	0.789 ± 0.090
Rotation	✓	24.9 ± 2.8	0.739 ± 0.089	28.8 ± 3.4	0.805 ± 0.080
	×	23.8 ± 2.9	0.668 ± 0.128	28.1 ± 3.5	0.766 ± 0.089

Table 4: Ablation study. Stopping the gradient is denoted with a checkmark ✓.

Method	Urban 100 [19]		CT [2]	
	PSNR	SSIM	PSNR	SSIM
Supervised	22.9 ± 1.9	0.702 ± 0.067	38.0 ± 0.6	0.953 ± 0.009
Proposed	22.7 ± 2.1	0.692 ± 0.066	34.3 ± 0.5	0.918 ± 0.009
CSS	20.9 ± 2.0	0.559 ± 0.077	29.7 ± 0.5	0.864 ± 0.012
PnP [42]	20.8 ± 1.9	0.546 ± 0.090	33.1 ± 0.5	0.912 ± 0.012
BM3D [11]	20.4 ± 1.8	0.512 ± 0.091	30.9 ± 0.5	0.887 ± 0.012
DIP [39]	19.9 ± 1.7	0.453 ± 0.074	28.3 ± 0.6	0.693 ± 0.024

Table 5: Reconstruction performance on other datasets.

hyper-parameters for every image in the dataset for fair comparison. For image deblurring, we compare against BM3D [11].

Box deblurring experiments Figure 3 shows that images obtained using the CSS method are blurrier than images obtained using the supervised and proposed methods, for all three blur levels. We observe horizontal and vertical artifacts on the image obtained using the supervised method for medium blur level, on those obtained using the proposed method for medium and high levels, and on those obtained using the CSS method for all three levels, but not on other images.

Table 1 shows that the proposed method performs better than the CSS method (+1.3 dB gain in average) and -1.1 dB worse than the supervised method. Overall, we observe that the proposed method performs almost as well as the supervised method, and better than the CSS method.

Gaussian deblurring experiments Figure 4 shows that the CSS method produces blurrier images than the supervised and proposed methods, for all three blur levels, and especially so for the two highest blur levels. For the highest blur level, we observe that the contour between two rocks on the upper right part of the zoomed-in region is visible on images obtained using the proposed and CSS methods, but is not visible on the image obtained using the supervised method.

Table 2 shows that the proposed method performs significantly better than the CSS method (+1.0 dB gain on average) and almost as good as the supervised method (-0.3 dB loss on average).

Super-resolution experiments For image super-resolution, Table 3 shows that the proposed method performs almost as well as the supervised method (about a .5 dB difference), and as predicted similarly as the CSS method. The wide variety of image pairs make DIP unlikely to perform well unless its hyper-parameters are tuned on an image-to-image basis and in this case it shows poor performance.

Even though the proposed and CSS methods have similar performance in average, Figure 5 shows that the CSS method can produce noisier images, perhaps due to the additional noise in training pairs. For easier comparison, zoomed in regions are displayed with increased luminosity.

Ablation study We compare the proposed method (using scale transforms) with equivariant imaging (using shift and rotation transforms), with and without stopping the gradient. Table 4 shows that the proposed method has better performance than equivariant imaging for both Gaussian deblurring with blur level $R_{\text{blur}} = 2$ and noise level $\sigma = 5/255$ and $\times 2$ super-resolution with noise level $\sigma = 25/255$. Moreover, it shows that stopping the gradient improves the reconstruction performance by about 1dB for all methods.

Other datasets In order to show how the proposed method preforms on different image distributions, we prepare a synthetic dataset with ground truth images from the Urban 100 dataset [19], and another one using a dataset of CT scans [2]. In both cases, we use a box kernel with blur level $R_{\text{blur}} = 3$ and Gaussian noise

with noise level $\sigma = 5/255$. In addition to other methods, we compare against the Plug-and-Play method (PnP) and use a denoising model trained using all 900 images from Div2K [42]. Table 5 shows that the proposed method performs slightly less than the supervised method for both datasets and significantly better than other methods.

6 Conclusion

In this work, we propose a new self-supervised method for solving the problems of image super-resolution and image deblurring which leverages the scale-invariance of typical image distributions. The experiments show that our method can be as effective as supervised methods while outperforming other self-supervised methods including Plug-and-Play, Deep Image Prior and BM3D.

The proposed method extends the equivariant imaging loss to image deblurring and image super-resolution, two problems where high-frequency information is lost which play a fundamental role in most imaging systems. The proposed method offers significant flexibility: i) the self-supervised loss can be used to train any network architecture, ii) the loss can be applied to many problems, e.g. upscaling natural images, deblurring CT scans, as long as the forward process is known, and iii) measurements through only one operator are needed as opposed to multi-operator techniques.

While a theoretical analysis of necessary and sufficient conditions for learning from measurement data alone is available for the case where the transformations T_g are associated with a compact group, such as rotations and/or translations [36], the results do not hold for the action by scalings which form a semi-group [40] (as it does not have an inverse). The interesting question of what theoretical conditions would enable model identification in this scenario is left for future work.

References

1. Agustsson, E., Timofte, R.: NTIRE 2017 Challenge on Single Image Super-Resolution: Dataset and Study. In: 2017 IEEE Conference on Computer Vision and Pattern Recognition Workshops (CVPRW). pp. 1122–1131. IEEE, Honolulu, HI, USA (Jul 2017). <https://doi.org/10.1109/CVPRW.2017.150>, <http://ieeexplore.ieee.org/document/8014884/>
2. Armato III, S.G., McLennan, G., Bidaut, L., McNitt-Gray, M.F., Meyer, C.R., Reeves, A.P., Zhao, B., Aberle, D.R., Henschke, C.I., Hoffman, E.A., et al.: The lung image database consortium (lidc) and image database resource initiative (idri): a completed reference database of lung nodules on ct scans. *Medical physics* **38**(2), 915–931 (2011)
3. Batson, J., Royer, L.: Noise2Self: Blind Denoising by Self-Supervision. In: Proceedings of the 36th International Conference on Machine Learning. pp. 524–533. PMLR (May 2019), <https://proceedings.mlr.press/v97/batson19a.html>, ISSN: 2640-3498

4. Belthangady, C., Royer, L.A.: Applications, promises, and pitfalls of deep learning for fluorescence image reconstruction. *Nature methods* **16**(12), 1215–1225 (2019)
5. Blau, Y., Michaeli, T.: The perception-distortion tradeoff. In: *Proceedings of the IEEE conference on computer vision and pattern recognition*. pp. 6228–6237 (2018)
6. Bora, A., Price, E., Dimakis, A.G.: Ambientgan: Generative models from lossy measurements. In: *International conference on learning representations* (2018)
7. Chambolle, A., Pock, T.: An introduction to continuous optimization for imaging. *Acta Numerica* **25**, 161–319 (2016)
8. Chen, D., Tachella, J., Davies, M.E.: Equivariant Imaging: Learning Beyond the Range Space. In: 2021 IEEE/CVF International Conference on Computer Vision (ICCV). pp. 4359–4368. IEEE, Montreal, QC, Canada (Oct 2021). <https://doi.org/10.1109/ICCV48922.2021.00434>, <https://ieeexplore.ieee.org/document/9711083/>
9. Chen, D., Tachella, J., Davies, M.E.: Robust Equivariant Imaging: a fully unsupervised framework for learning to image from noisy and partial measurements. In: 2022 IEEE/CVF Conference on Computer Vision and Pattern Recognition (CVPR). pp. 5637–5646. IEEE, New Orleans, LA, USA (Jun 2022). <https://doi.org/10.1109/CVPR52688.2022.00556>, <https://ieeexplore.ieee.org/document/9880116/>
10. Chen, X., He, K.: Exploring Simple Siamese Representation Learning (Nov 2020). <https://doi.org/10.48550/arXiv.2011.10566>, <http://arxiv.org/abs/2011.10566>, arXiv:2011.10566 [cs]
11. Dabov, K., Foi, A., Katkovnik, V., Egiazarian, K.: Image denoising by sparse 3-d transform-domain collaborative filtering. *IEEE Transactions on image processing* **16**(8), 2080–2095 (2007)
12. Darestani, M.Z., Heckel, R.: Accelerated mri with un-trained neural networks. *IEEE Transactions on Computational Imaging* **7**, 724–733 (2021)
13. Dong, J., Roth, S., Schiele, B.: Deep Wiener Deconvolution: Wiener Meets Deep Learning for Image Deblurring. In: *Advances in Neural Information Processing Systems*. vol. 33, pp. 1048–1059. Curran Associates, Inc. (2020), <https://proceedings.neurips.cc/paper/2020/hash/0b8aff0438617c055eb55f0ba5d226fa-Abstract.html>
14. Eldar, Y.C.: Generalized SURE for Exponential Families: Applications to Regularization. *IEEE Transactions on Signal Processing* **57**(2), 471–481 (Feb 2009). <https://doi.org/10.1109/TSP.2008.2008212>, <https://ieeexplore.ieee.org/abstract/document/4663926>, conference Name: IEEE Transactions on Signal Processing
15. Fatania, K., Chau, K.Y., Pirkel, C.M., Menzel, M.I., Golbabaee, M.: Non-linear Equivariant Imaging: Learning Multi-Parametric Tissue Mapping without Ground Truth for Compressive Quantitative MRI. In: 2023 IEEE 20th International Symposium on Biomedical Imaging (ISBI). pp. 1–4 (Apr 2023). <https://doi.org/10.1109/ISBI53787.2023.10230440>, https://ieeexplore.ieee.org/abstract/document/10230440?casa_token=3g3pZii4X14AAAAA:oIdWkoBtVELL6ohhLoBtKzWeQvwSvTSMJphpmND0V91R7WBM_fXTvKT1QIsaQhogjU0hA, iSSN: 1945-8452
16. Florack, L.M., ter Haar Romeny, B.M., Koenderink, J.J., Viergever, M.A.: Scale and the differential structure of images. *Image and vision computing* **10**(6), 376–388 (1992)
17. Grill, J.B., Strub, F., Althé, F., Tallec, C., Richemond, P.H., Buchatskaya, E., Doersch, C., Pires, B.A., Guo, Z.D., Azar, M.G., Piot, B., Kavukcuoglu, K., Munos,

- R., Valko, M.: Bootstrap Your Own Latent A New Approach to Self-Supervised Learning
18. Hendriksen, A.A., Pelt, D.M., Batenburg, K.J.: Noise2Inverse: Self-supervised deep convolutional denoising for tomography. *IEEE Transactions on Computational Imaging* **6**, 1320–1335 (2020). <https://doi.org/10.1109/TCI.2020.3019647>, <http://arxiv.org/abs/2001.11801>, arXiv:2001.11801 [cs, eess, stat]
 19. Huang, J.B., Singh, A., Ahuja, N.: Single image super-resolution from transformed self-exemplars. In: 2015 IEEE Conference on Computer Vision and Pattern Recognition (CVPR). pp. 5197–5206. IEEE, Boston, MA, USA (Jun 2015). <https://doi.org/10.1109/CVPR.2015.7299156>, <http://ieeexplore.ieee.org/document/7299156/>
 20. Kamilov, U.S., Bouman, C.A., Buzzard, G.T., Wohlberg, B.: Plug-and-play methods for integrating physical and learned models in computational imaging: Theory, algorithms, and applications. *IEEE Signal Processing Magazine* **40**(1), 85–97 (2023)
 21. Kingma, D.P., Ba, J.: Adam: A method for stochastic optimization. arXiv preprint arXiv:1412.6980 (2014)
 22. Krull, A., Buchholz, T.O., Jug, F.: Noise2Void - Learning Denoising From Single Noisy Images. pp. 2129–2137 (2019), https://openaccess.thecvf.com/content_CVPR_2019/html/Krull_Noise2Void_-_Learning_Denoising_From_Single_Noisy_Images_CVPR_2019_paper.html
 23. Lehtinen, J., Munkberg, J., Hasselgren, J., Laine, S., Karras, T., Aittala, M., Aila, T.: Noise2Noise: Learning Image Restoration without Clean Data. In: Proceedings of the 35th International Conference on Machine Learning. pp. 2965–2974. PMLR (Jul 2018), <https://proceedings.mlr.press/v80/lehtinen18a.html>, iSSN: 2640-3498
 24. Liang, J., Cao, J., Sun, G., Zhang, K., Van Gool, L., Timofte, R.: SwinIR: Image Restoration Using Swin Transformer. In: 2021 IEEE/CVF International Conference on Computer Vision Workshops (ICCVW). pp. 1833–1844. IEEE, Montreal, BC, Canada (Oct 2021). <https://doi.org/10.1109/ICCVW54120.2021.00210>, <https://ieeexplore.ieee.org/document/9607618/>
 25. Ma, K., Duanmu, Z., Wu, Q., Wang, Z., Yong, H., Li, H., Zhang, L.: Waterloo exploration database: New challenges for image quality assessment models. *IEEE Transactions on Image Processing* **26**(2), 1004–1016 (2016)
 26. Mataev, G., Milanfar, P., Elad, M.: DeepRED: Deep Image Prior Powered by RED. pp. 0–0 (2019), https://openaccess.thecvf.com/content_ICCVW_2019/html/Mataev_DeepRED_Deep_Image_Prior_Powered_by_RED_ICCVW_2019_paper.html
 27. Metzler, C.A., Mousavi, A., Heckel, R., Baraniuk, R.G.: Unsupervised Learning with Stein’s Unbiased Risk Estimator (Jul 2020). <https://doi.org/10.48550/arXiv.1805.10531>, <http://arxiv.org/abs/1805.10531>, arXiv:1805.10531 [cs, stat]
 28. Moran, N., Schmidt, D., Zhong, Y., Coady, P.: Noisier2noise: Learning to denoise from unpaired noisy data. In: Proceedings of the IEEE/CVF Conference on Computer Vision and Pattern Recognition. pp. 12064–12072 (2020)
 29. Quan, Y., Chen, Z., Zheng, H., Ji, H.: Learning Deep Non-blind Image Deconvolution Without Ground Truths. In: Avidan, S., Brostow, G., Cissé, M., Farinella, G.M., Hassner, T. (eds.) *Computer Vision – ECCV 2022*. pp. 642–659. Lecture Notes in Computer Science, Springer Nature Switzerland, Cham (2022). https://doi.org/10.1007/978-3-031-20068-7_37

30. Quemener, E., Corvellec, M.: Sidus—the solution for extreme deduplication of an operating system. *Linux Journal* **2013**(235), 3 (2013). <https://doi.org/https://dl.acm.org/doi/abs/10.5555/2555789.2555792>
31. Ramani, S., Blu, T., Unser, M.: Monte-carlo sure: A black-box optimization of regularization parameters for general denoising algorithms. *IEEE Transactions on image processing* **17**(9), 1540–1554 (2008)
32. Ren, D., Zhang, K., Wang, Q., Hu, Q., Zuo, W.: Neural blind deconvolution using deep priors. In: *Proceedings of the IEEE/CVF Conference on Computer Vision and Pattern Recognition*. pp. 3341–3350 (2020)
33. Ren, W., Zhang, J., Ma, L., Pan, J., Cao, X., Zuo, W., Liu, W., Yang, M.H.: Deep Non-Blind Deconvolution via Generalized Low-Rank Approximation. In: *Advances in Neural Information Processing Systems*. vol. 31. Curran Associates, Inc. (2018), <https://proceedings.neurips.cc/paper/2018/hash/0aa1883c6411f7873cb83dacb17b0afc-Abstract.html>
34. Shocher, A., Cohen, N., Irani, M.: Zero-Shot Super-Resolution Using Deep Internal Learning. In: *2018 IEEE/CVF Conference on Computer Vision and Pattern Recognition*. pp. 3118–3126. IEEE, Salt Lake City, UT (Jun 2018). <https://doi.org/10.1109/CVPR.2018.00329>, <https://ieeexplore.ieee.org/document/8578427/>
35. Stein, C.M.: Estimation of the Mean of a Multivariate Normal Distribution. *The Annals of Statistics* **9**(6), 1135–1151 (1981), <https://www.jstor.org/stable/2240405>, publisher: Institute of Mathematical Statistics
36. Tachella, J., Pereyra, M.: Equivariant Bootstrapping for Uncertainty Quantification in Imaging Inverse Problems (Oct 2023). <https://doi.org/10.48550/arXiv.2310.11838>, <http://arxiv.org/abs/2310.11838>, arXiv:2310.11838 [cs, eess, stat]
37. Tachella, J., Chen, D., Davies, M.: Sensing Theorems for Unsupervised Learning in Linear Inverse Problems. *Journal of Machine Learning Research* **24**(39), 1–45 (2023), <http://jmlr.org/papers/v24/22-0315.html>
38. Timofte, R., Agustsson, E., Van Gool, L., Yang, M.H., Zhang, L.: Ntire 2017 challenge on single image super-resolution: Methods and results. In: *Proceedings of the IEEE conference on computer vision and pattern recognition workshops*. pp. 114–125 (2017)
39. Ulyanov, D., Vedaldi, A., Lempitsky, V.: Deep Image Prior. pp. 9446–9454 (2018), https://openaccess.thecvf.com/content_cvpr_2018/html/Ulyanov_Deep_Image_Prior_CVPR_2018_paper.html
40. Worrall, D., Welling, M.: Deep scale-spaces: Equivariance over scale. *Advances in Neural Information Processing Systems* **32** (2019)
41. Xu, L., Ren, J.S., Liu, C., Jia, J.: Deep Convolutional Neural Network for Image Deconvolution. In: *Advances in Neural Information Processing Systems*. vol. 27. Curran Associates, Inc. (2014), <https://proceedings.neurips.cc/paper/2014/hash/1c1d4df596d01da60385f0bb17a4a9e0-Abstract.html>
42. Zhang, K., Zuo, W., Gu, S., Zhang, L.: Learning deep cnn denoiser prior for image restoration. In: *Proceedings of the IEEE conference on computer vision and pattern recognition*. pp. 3929–3938 (2017)

A Implementation details

Deep Image Prior We use a learning rate of $\lambda = 5 \cdot 10^{-3}$, an input size of 16×16 with 32 channels using a convolutional decoder network architecture [12].

Plug-and-Play We use the method described in [42] with 100 iterations and early stopping, using a denoiser pre-trained on 400 images from the BSD dataset, 900 images from the Div2K dataset [1], 4,744 images from the Waterloo Exploration Database [25] and 2,750 images from the Flick2K dataset [38].

B Additional figures

Figures 6 to 8 each shows reconstructions for another sample image, respectively for box deblurring, Gaussian deblurring and image super-resolution.

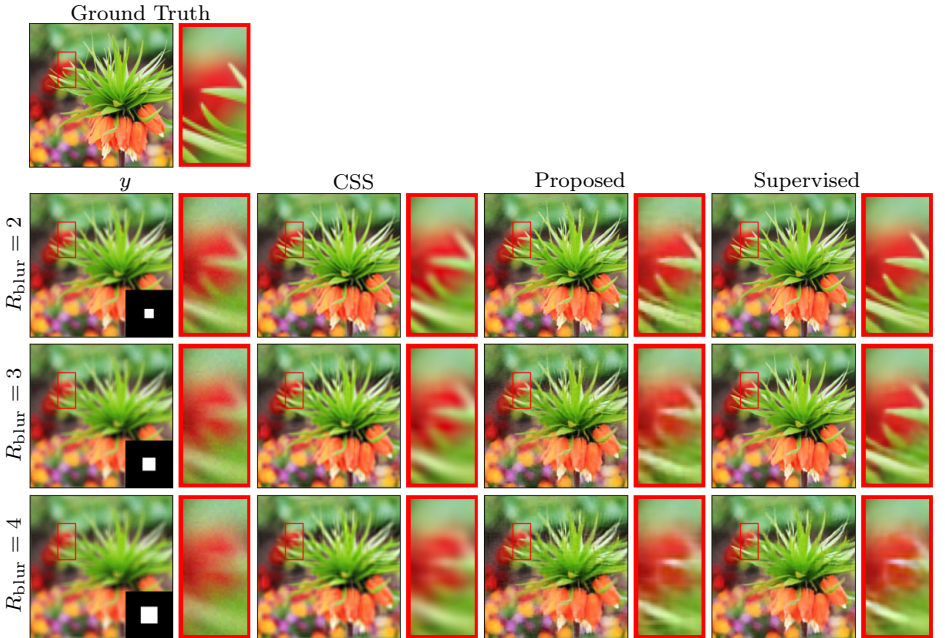


Fig. 6: Additional sample reconstructions for box deblurring.

C Proofs of Proposition 1 and 2

In this section, we provide proofs for Proposition 1 and 2. For the sake of simplicity, we consider images $x \in \mathbb{R}^n$ with height and width equal to $n' = \sqrt{n}$, although

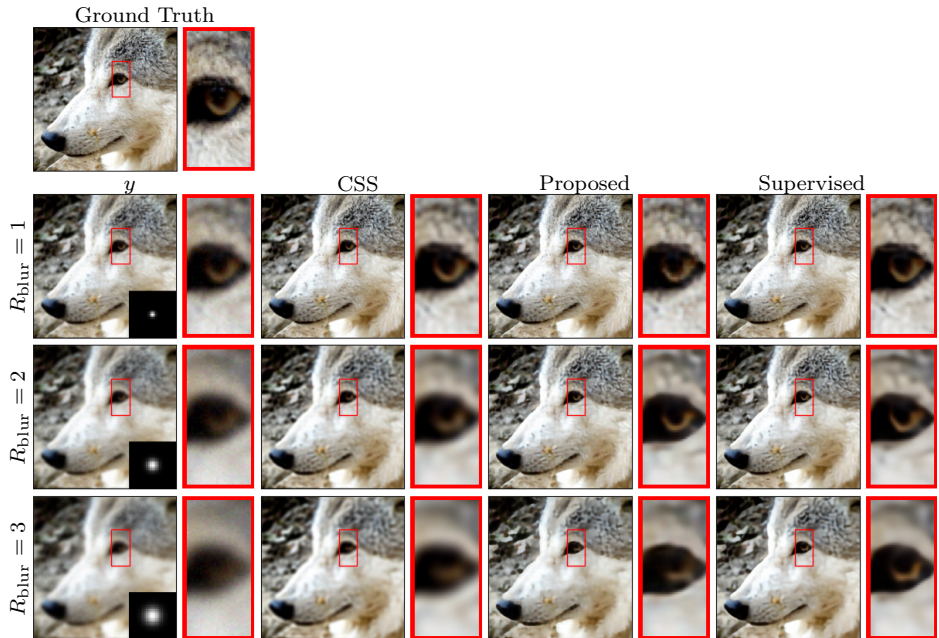


Fig. 7: Additional sample reconstructions for Gaussian deblurring.

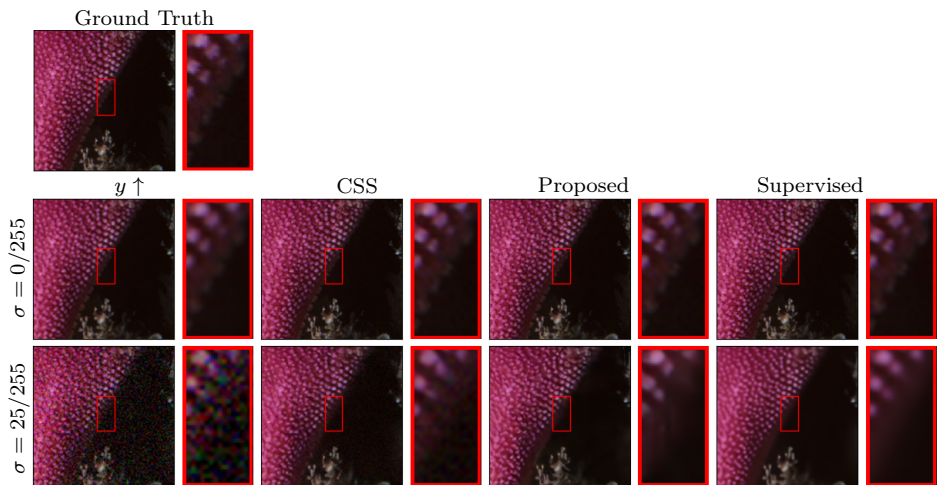


Fig. 8: Additional sample reconstructions for $\times 2$ image super-resolution.

the results can be generalized for any aspect ratio. Furthermore, we write $x_{l,s} \in \mathbb{R}$ to denote the pixel in the (l, s) th coordinate of x , where $l = 0, 1, \dots, n' - 1$ and $s = 0, 1, \dots, n' - 1$.

Discrete Fourier transform We use the spectral properties of downsampling with an ideal low-pass filter, expressed in terms of the 2D discrete Fourier transform $\mathcal{F} \in \mathbb{C}^{n \times n}$ defined by

$$(\mathcal{F}x)_{l,s} = \sum_{p=0}^{n'-1} \sum_{q=0}^{n'-1} x_{p,q} e^{-2i\pi(lp+sq)/n'} \quad (10)$$

where $l, s = 0, \dots, n' - 1$.

2D circular convolutions In order to define blur and downsampling operators, we use the 2D circular convolution of a signal $x \in \mathbb{R}^n$ by a kernel $k \in \mathbb{R}^n$, defined by

$$(k * x)_{l,s} = \sum_{p=0}^{n'-1} \sum_{q=0}^{n'-1} k_{p,q} x_{(l-p)_{n'}, (s-q)_{n'}}, \quad (11)$$

where $l, s = 0, \dots, n' - 1$, and $(l - p)_{n'}$ denotes the remainder of $l - p$ divided by n' .

Blur and downsampling operators In this section, we consider a blur operator $B \in \mathbb{R}^{n \times n}$, defined as the 2D circular convolution by kernel $k \in \mathbb{R}^n$,

$$Bx = k * x, \quad x \in \mathbb{R}^n, \quad (12)$$

and a downsampling operator $S \in \mathbb{R}^{m \times n}$, defined by

$$(Sx)_{l,s} = (k * x)_{rl,rs}, \quad x \in \mathbb{R}^n,$$

where $r = n'/m'$ is the downsampling factor, $m' = \sqrt{m}$, $k \in \mathbb{R}^n$ is an antialiasing kernel and $l, s = 0, \dots, m' - 1$. Without loss of generality, we focus on downsampling by a factor of 2, i.e. $m' = n'/2$ and $r = 2$, however, our results can easily be generalized for other integer factors.

Actions by shifts and rotations The action by shifts $T_{g_1, g_2} \in \mathbb{R}^{n \times n}$, with horizontal and vertical displacements $g_1, g_2 = 0, \dots, n' - 1$, is defined by

$$(T_{g_1, g_2} x)_{l,s} = x_{(l+g_1)_{n'}, (s+g_2)_{n'}}, \quad x \in \mathbb{R}^n, \quad (13)$$

where $l, s = 0, \dots, n' - 1$, or equivalently in the Fourier basis

$$(\hat{T}_{g_1, g_2} \hat{x})_{l,s} = e^{2i\pi(lg_1 + sg_2)/n'} \hat{x}_{l,s}, \quad (14)$$

where $\hat{T}_{g_1, g_2} = \mathcal{F} T_{g_1, g_2} \mathcal{F}^{-1} \in \mathbb{R}^{n \times n}$.

The action by rotations $R_g \in \mathbb{R}^{n \times n}$, with angles of $g = 0, 90, 180, 270$ degrees, is defined by

$$(R_g x)_{l,s} = \begin{cases} x_{(l)_{n'},(s)_{n'}} & \text{if } g = 0, \\ x_{(-s)_{n'},(l)_{n'}} & \text{if } g = 90, \\ x_{(-l)_{n'},(-s)_{n'}} & \text{if } g = 180, \\ x_{(s)_{n'},(-l)_{n'}} & \text{if } g = 270, \end{cases} \quad (15)$$

where $l, s = 0, \dots, n' - 1$.

Equivariance to shifts and rotations In this section, we prove that under mild conditions the blur operator B and the downsampling operator S are equivariant to actions by shifts T_g , and by rotations R_g . Because equivariance is a property relating an operator and a group acting on both its input and output spaces, we need to specify what group action on the output space we consider in each case. For the blur operator B , input and output spaces are equal, and we consider the action on its output space to be equal to the action on its input space.

For operator S and action by rotations R_g , we consider the action on the output space to be the action by rotations $\tilde{R}_g \in \mathbb{R}^{m \times m}$, $g = 0, 90, 180, 270$, and for the action by shifts T_g , we consider the action on the output space to be the translation by a displacement of $g/2$, defined in Fourier basis by

$$(\hat{T}_{g_1, g_2} \hat{x})_{l,s} = e^{2i\pi(lg_1/2 + sg_2/2)/m'} \hat{x}_{l,s}. \quad (16)$$

In summary, we will prove that

$$BR_g = R_g B \quad \text{for } g = 0, 90, 180, 270 \quad (17)$$

$$SR_g = \tilde{R}_g S \quad \text{for } g = 0, 90, 180, 270 \quad (18)$$

$$BT_{g_1, g_2} = T_{g_1, g_2} B \quad \text{for } g_1, g_2 = 0, \dots, n' - 1 \quad (19)$$

$$ST_{g_1, g_2} = \tilde{T}_{g_1, g_2} S \quad \text{for } g_1, g_2 = 0, \dots, n' - 1. \quad (20)$$

Isotropic kernels An isotropic kernel $k \in \mathbb{R}^n$ is a kernel that is invariant to rotations, in our case it satisfies

$$R_g k = k, \quad g = 0, 90, 180, 270. \quad (21)$$

Ideal anti-aliasing filter A downsampling operator S by factor 2 with ideal anti-aliasing filter $k \in \mathbb{R}^n$ satisfies

$$(\hat{S}\hat{x})_{(l)_{m'},(s)_{m'}} = (\hat{x})_{(l)_{n'},(s)_{n'}}, \quad (22)$$

where $l, s = -(m' - 1)/2, \dots, (m' - 1)/2$, assuming n' is even and m' is odd.

C.1 Proof of Proposition 1

We prove the proposition in two steps, first by proving that the blur operator is equivariant to shifts, then that it is equivariant to rotations as long as the kernel is isotropic.

Let $x \in \mathbb{R}^n$ and $g_1, g_2 = 0, \dots, n' - 1$. Using (12) and Lemma 1, we compute

$$BT_{g_1, g_2}x = k * (T_{g_1, g_2}x) \quad (23)$$

$$= T_{g_1, g_2}(k * x) \quad (24)$$

$$= T_{g_1, g_2}Bx. \quad (25)$$

Thus the blur operator is equivariant to shifts.

Now, we assume that k is an isotropic kernel, and let $g = 0, 90, 180, 270$. Using (12) and Lemma 2 we compute

$$BR_gx = (k * (R_gx)), \quad (26)$$

$$= R_g(R_{g'}k * x), \quad (27)$$

where $g' = (360 - g)_{n'}$. Then using (21) and (12) we compute

$$BR_gx = R_g(k * x) \quad (28)$$

$$= R_gBx. \quad (29)$$

Thus the blur operator is equivariant to shifts.

Lemma 1. For $x, k \in \mathbb{R}^n$, and $g_1, g_2 = 0, \dots, n' - 1$

$$k * (T_{g_1, g_2}x) = T_{g_1, g_2}(k * x). \quad (30)$$

Proof. Let $l, s = 0, \dots, n' - 1$,

$$[k * (T_{g_1, g_2}x)]_{l, s} = \sum_{p=0}^{n'-1} \sum_{q=0}^{n'-1} k_{p, q} [T_{g_1, g_2}x]_{(l-p)_{n'}, (s-q)_{n'}} \quad (31)$$

$$= \sum_{p=0}^{n'-1} \sum_{q=0}^{n'-1} k_{p, q} x_{(l+g_1-p)_{n'}, (s+g_2-q)_{n'}} \quad (32)$$

$$= (k * x)_{l+g_1, s+g_2} \quad (33)$$

$$= [T_{g_1, g_2}(k * x)]_{l, s}. \quad (34)$$

Lemma 2. For $k, x \in \mathbb{R}^n$, and $g = 0, 90, 180, 270$,

$$k * (R_gx) = R_g(R_{g'}k * x), \quad (35)$$

where $g' = (360 - g)_{360}$.

Proof. We prove the four cases separately. First, if $g = 0$, then $g' = 0$, $R_g = R_{g'} = I_n$, and (35) is satisfied. If $g = 90$, then $g' = 270$, and using (11) and (15)

we compute

$$(R_g((R_{g'}k) * x))_{l,s} = ((R_{g'}k) * x)_{(-s)_{n'},(l)_{n'}} \quad (36)$$

$$= \sum_{p=0}^{n'-1} \sum_{q=0}^{n'-1} (R_{g'}k)_{p,q} x_{(-s-p)_{n'},(l-q)_{n'}} \quad (37)$$

$$= \sum_{p=0}^{n'-1} \sum_{q=0}^{n'-1} k_{(q)_{n'},(-p)_{n'}} x_{(-s-p)_{n'},(l-q)_{n'}} \quad (38)$$

$$= \sum_{p=0}^{n'-1} \sum_{q=0}^{n'-1} k_{(q)_{n'},(p)_{n'}} x_{(-s+p)_{n'},(l-q)_{n'}} \quad (39)$$

$$= \sum_{p=0}^{n'-1} \sum_{q=0}^{n'-1} k_{p,q} x_{(-s+q)_{n'},(l-p)_{n'}} \quad (40)$$

$$= \sum_{p=0}^{n'-1} \sum_{q=0}^{n'-1} k_{p,q} (R_g x)_{(l-p)_{n'},(s-q)_{n'}} \quad (41)$$

$$= (k * (R_g x))_{l,s}. \quad (42)$$

The cases $g = 180$ and $g = 270$ are proven similarly.

C.2 Proof of Proposition 2

We start by proving that the downsampling operator with anti-aliasing filter is equivariant to shifts, then we prove it is equivariant to rotations.

Let $x \in \mathbb{R}^n$, $g_1, g_2 = 0, \dots, n' - 1$, and $l, s = -(m' - 1)/2, \dots, (m' - 1)/2$. Using (22), (14) and (16) we compute

$$(\hat{S}\hat{T}_{g_1, g_2}\hat{x})_{(l)_{m'}, (s)_{m'}} = (\hat{T}_{g_1, g_2}\hat{x})_{(l)_{n'}, (s)_{n'}} \quad (43)$$

$$= e^{2i\pi(lg_1 + sg_2)/n'} \hat{x}_{(l)_{n'}, (s)_{n'}} \quad (44)$$

$$= e^{2i\pi(lg_1/2 + sg_2/2)/m'} (\hat{S}\hat{x})_{l,s} \quad (45)$$

$$= (\hat{T}_{g_1, g_2}\hat{S}\hat{x})_{l,s}. \quad (46)$$

Thus, the operator is equivariant to shifts.

Let $g = 0, 90, 180, 270$, and $l, s = -(m' - 1)/2, \dots, (m' - 1)/2$. Using (22), Lemma 3 and Lemma 4, we compute

$$(\hat{S}\hat{R}_g\hat{x})_{(l)_{m'},(s)_{m'}} = (\hat{R}_g\hat{x})_{(l)_{n'},(s)_{n'}} \quad (47)$$

$$= (R_g\hat{x})_{(l)_{n'},(s)_{n'}} \quad (48)$$

$$= (\tilde{R}_g\hat{S}\hat{x})_{(l)_{m'},(s)_{m'}} \quad (49)$$

$$= (\tilde{R}_g\hat{S}\hat{x})_{(l)_{n'},(s)_{n'}} \quad (50)$$

$$= (\hat{\tilde{R}}_g\hat{S}\hat{x})_{(l)_{n'},(s)_{n'}}. \quad (51)$$

Thus, the operator is equivariant to rotations.

Lemma 3. For $g = 0, 90, 180, 270$

$$\hat{R}_g = R_g. \quad (52)$$

where $\hat{R}_g = \mathcal{F}R_g\mathcal{F}^{-1}$.

Proof. If $g = 0$, then $R_g = I_n$ and (52) is satisfied. If $g = 90$, let $x \in \mathbb{R}^n$, and $l, s = 0, \dots, n' - 1$. We compute

$$(\hat{R}_g\hat{x})_{l,s} = (\mathcal{F}R_gx)_{l,s} \quad (53)$$

$$= \sum_{p=0}^{n'-1} \sum_{q=0}^{n'-1} (R_gx)_{p,q} e^{-2i\pi(lp+sq)/n'} \quad (54)$$

$$= \sum_{p=0}^{n'-1} \sum_{q=0}^{n'-1} x_{(-q)_{n'},(p)_n} e^{-2i\pi(lp+sq)/n'} \quad (55)$$

$$= \sum_{p=0}^{n'-1} \sum_{q=0}^{n'-1} x_{p,q} e^{-2i\pi(-sp+lq)/n'} \quad (56)$$

$$= (\hat{x})_{(-s)_{n'},(l)_{n'}} \quad (57)$$

$$= (R_g\hat{x})_{l,s} \quad (58)$$

thus $\hat{R}_g = R_g$. If $g = 180$ or $g = 270$, we prove $\hat{R}_g = R_g$ similarly as in the $g = 90$ case.

Lemma 4. For $g = 0, 90, 180, 270$, $x \in \mathbb{R}^n$, and $l, s = -(m' - 1)/2, \dots, (m' - 1)/2$,

$$(R_g\hat{x})_{(l)_{n'},(s)_{n'}} = (\tilde{R}_g\hat{S}\hat{x})_{(l)_{m'},(s)_{m'}}. \quad (59)$$

Proof. For $g = 0$, $R_g = I_n$ and $\tilde{R}_g = I_m$, then using (22) we obtain (59). If $g = 90$, we compute

$$(R_g\hat{x})_{(l)_{n'},(s)_{n'}} = (\hat{x})_{(-s)_{n'},(l)_{n'}} \quad (60)$$

$$= (\hat{S}\hat{x})_{(-s)_{m'},(l)_{m'}} \quad (61)$$

$$= (\tilde{R}_g\hat{S}\hat{x})_{(l)_{m'},(s)_{m'}}. \quad (62)$$

The cases $g = 180$ and $g = 270$ can be proven similarly.

D Proof of Theorem 1

In this section, we prove that blurring and downsampling with an ideal anti-aliasing filter is not equivariant to downscaling. Since an ideal anti-aliasing filter is a special case of blurring operator, it suffices to prove that blurring is not equivariant to downscaling, i.e. that for a signal $x \in \mathbb{R}^n$, and a scaling factor $g \in \{1/2, 1/3, \dots\}$,

$$AT_g x \neq T_g A x. \quad (63)$$

Without loss of generality, we prove the theorem for 1D signals. Extending the results to 2D signals is straightforward.

Blur transfer function The Fourier transform of a blur filter is typically nonzero around the zero-frequency, and in particular as long as the number of samples n is large enough,

$$\hat{a}_1 \neq 0. \quad (64)$$

Moreover, if the blur operator is not invertible, its Fourier transform \hat{a} vanishes for some frequency $0 < 1/g < n/2$,

$$\hat{a}_{1/g} = 0. \quad (65)$$

Symmetry of real filters Throughout the proof, we use the symmetry property of real filters (note that we work with real forward operators A), which satisfy

$$\hat{a}_l = \bar{\hat{a}}_{(n-l)_n}, \quad l = 0, \dots, n-1 \quad (66)$$

where \bar{z} denote the complex conjugate of $z \in \mathbb{C}$.

Action by downscalings Downscaling in space is equivalent to upscaling in frequency and the downscaling T_g by a factor $g \in \{1/2, 1/3, \dots\}$ satisfies

$$\hat{T}_g(\alpha\delta^{(1)} + \beta\delta^{(n-1)}) = \alpha\delta^{(1/g)} + \beta\delta^{(n-1/g)} \quad (67)$$

where $\alpha, \beta \in \mathbb{C}$, and $\delta^{(l)}$ is a Dirac vector positioned at l , i.e. $\delta_s^{(l)} = 1$ if $l = s$, and $\delta_s^{(l)} = 0$ otherwise.

D.1 Proof

Consider a sinusoidal signal $x \in \mathbb{R}^n$ with Fourier transform

$$\hat{x} = \delta^{(1)} + \delta^{(n-1)}. \quad (68)$$

We begin by showing that

$$AT_g x = 0. \quad (69)$$

Letting $y^{(1)} := AT_g x$ and using (65), we have that

$$\begin{aligned}
 \hat{y}^{(1)} &= \hat{a} \odot \hat{T}_g \hat{x}^{(1)} \\
 &= \hat{a} \odot \hat{T}_g (\delta^{(1)} + \delta^{(n-1)}) \\
 &= \hat{a} \odot (\delta^{(1/g)} + \delta^{(n-1/g)}) \\
 &= \hat{a}_{1/g} \delta^{(1/g)} + \hat{a}_{n-1/g} \delta^{(n-1/g)} \\
 &= \hat{a}_{1/g} \delta^{(1/g)} + \bar{\hat{a}}_{1/g} \delta^{(n-1/g)} \\
 &= 0.
 \end{aligned}$$

Next we show that

$$T_g Ax \neq 0. \quad (70)$$

Letting $y^{(2)} := T_g Ax$ and using (64), we obtain

$$\begin{aligned}
 \hat{y}^{(2)} &= \hat{T}_g (\hat{a} \odot \hat{x}) \\
 &= \hat{T}_g (\hat{a} \odot (\delta^{(1)} + \delta^{(n-1)})) \\
 &= \hat{T}_g (\hat{a}_1 \delta^{(1)} + \hat{a}_{n-1} \delta^{(n-1)}) \\
 &= \hat{a}_1 \delta^{(1/g)} + \hat{a}_{n-1} \delta^{(n-1/g)} \\
 &= \hat{a}_1 \delta^{(1/g)} + \bar{\hat{a}}_1 \delta^{(n-1/g)} \\
 &\neq 0.
 \end{aligned}$$

In conclusion,

$$AT_g x = y^{(1)} = 0 \neq y^{(2)} = T_g Ax, \quad (71)$$

and in particular A is not equivariant to downscalings.